J. Fluid Mech. (1982), *vol.* 123, *pp.* 237–265
Printed in Great Britain

The intrusion of a density current along the coast of a rotating fluid

By MELVIN E. STERN,
Graduate School of Oceanography, University of Rhode Island

JOHN A. WHITEHEAD
Woods Hole Oceanographic Institution

AND BACH-LIEN HUA
Museum National d'Histoire Naturelle, Paris

(Received 19 June 1981 and in revised form 25 February 1982)

When light rotating fluid spreads over heavier fluid in the vicinity of a vertical wall (coast) a boundary jet of width $\hat{L}$ forms, the leading edge or nose of which propagates with speed $\hat{c}$ along the coast. A certain fraction δ of the boundary transport is not carried by the nose but is deflected backwards (detrained) and left behind the propagating nose. Theoretical and experimental results for $\hat{L}$, $\hat{c}$, and δ are given for a quasi-equilibrium (constant-$\hat{c}$) regime. Over longer time intervals the laboratory observations suggest that the nose slows down and stagnates, whereupon the trailing flow separates from the coast and an intermittent boundary current forms. These processes may be relevant to the mixing of oceanic coastal currents and the maintenance of the mean current.

1. Introduction and statement of the problem

The way in which rotation inhibits the lateral spreading and mixing of a density current is illustrated by the Rossby adjustment problem (Saunders 1973; Stern 1975, chap. III). In the initial state a circular cylinder of radius R, height H and density ρ is resting in a frame rotating with angular velocity $\frac{1}{2}f$, and is surrounded by a deep resting fluid of density $\rho+\Delta\rho$. Gravity then causes the cylinder of uniform potential vorticity f/H to collapse vertically and spread horizontally, with individual columns tending to conserve potential vorticity. A balanced geostrophic (cyclostrophic) vortex may then result, in which the surface front advances only a distance $\Delta R \sim (g^*H)^{\frac{1}{2}}f^{-1}$ of the order of the Rossby radius of deformation, where $g^* = g\Delta\rho/\rho$. The vortex may be unstable, and more than one vortex may form if the initial radius is large compared with ΔR (Griffiths & Linden 1981).

The adjustment and the overall mixing process is drastically altered, however, when there is a vertical wall (figure 1). Although the adjustment of the semi-infinite light fluid is essentially unaltered at *large* distances $\hat{y}$ from the wall, a boundary current near $\hat{y} = 0$ must develop to accommodate the geostrophic flow into the wall. This coastal current transports the light fluid away from its source region, and thereby allows mixing to occur over much greater distances than would occur without the boundary (Wadhams, Gill & Linden 1979). What is the width of the boundary current; what is the nature of the leading edge (nose) of the coastal intrusion; is the

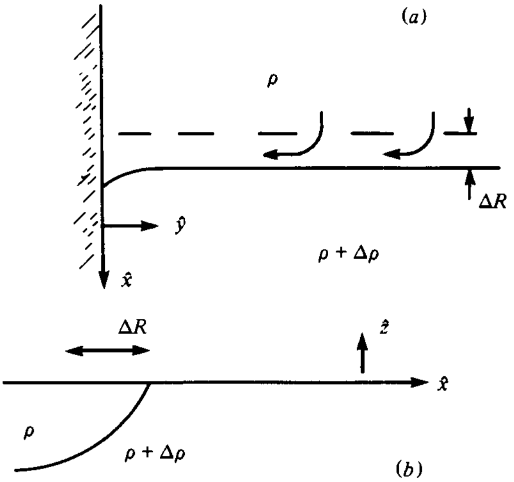

FIGURE 1. The initial stage in the rotating dam-break problem when a vertical wall ($\hat{y} = 0$) is present. The semi-infinite upper fluid has density ρ and the very deep lower layer has density $\rho+\Delta\rho$. The top view (a) shows the surface front advancing a distance ΔR at position far from the wall. But the geostrophic flow that develops runs into a wall stagnation point and a coastal intrusion must form. The vertical section (b) shows the equilibrium front far from the wall.

boundary current laminar, and if not, how does it mix into the adjacent water? These questions are addressed here by a combined theoretical and experimental study. The experiments (see §2) consist of lifting a vertical gate ('dam-break' experiment) which was initially in the position of the dashed line in figure 1. The thin layer of light water (ρ) in this figure then spread laterally and was deflected to the coast, where a boundary current finally emerged. The dimensional width $\hat{y}$ of the latter was measured, as well as the nose speed of the density current. Considerable *lateral* detrainment from the seaward portion of the nose was also observed, this effect being somewhat similar to the vertical detrainment through the interface of a non-rotating intrusion in a two-layer fluid (Britter & Simpson 1978; Simpson & Britter 1979). Benjamin (1968) has given a theory for the latter case, the experimental agreement being good in a limiting regime where the detrainment is relatively weak. Our theory of the rotating intrusion therefore begins (§3) with the generalization of Benjamin's theory. We do not, however, neglect the (experimentally) important detrainment effect. Another notable novelty of our problem is the additional horizontal dimension and structure of the fluid behind the bore. We identify those regions where the flow is approximately steady, and also those unsteady regions in which the important detrainment occurs. With these additional considerations Benjamin's theory for the nose speed will obviously not close, and additional constraints on the trailing current are necessary. For this purpose we advance (§4) a model and a similarity solution, which predicts an upstream width (cf. equations (4.31), (C 23)) for a so-called 'limiting bore' (Stern 1980) which agrees closely with experiment (equations (2.1), (2.2)). By combining the model with Benjamin's formula, a nose speed and detrainment coefficient are predicted which are also in acceptable agreement with experiments.

The reader should be warned, however, that the simple theory corresponds to a different *initial*-value problem than does the complex experiment, and it will be argued that a connection between the two exists at *later* times. In view of the admitted weakness of this argument, an alternative derivation of one main theoretical result, involving much weaker assumptions, is given in appendix A. This leads to an upper bound on the width of semi-permanent intrusions, and any wider initial state could not propagate along a coast before it suffered great alterations (e.g. bifurcation into a thin current which leaves the wide current behind).

2. The laboratory experiment

2.1 *Set-up and procedure*

Although the problem in which a heavy density current intrudes on the bottom of the rotating tank will have similar properties, it is experimentally more convenient to work with a surface intrusion so as to minimize Ekman friction and to eliminate topographic effects due to the slope of the bottom relative to the level parabolic surfaces.

The experiments were conducted in a rectangular tank which was made from Plexiglas one-half inch wide. The tank, sketched in figure 2, was 183 cm long, 29·2 cm deep, and 20 cm wide (inside dimensions). Grooves were cut into the sides and bottom of the tank at various places in order to allow a sliding gate, of 22-gauge stainless steel, to divide the tank into two chambers. The grooves were approximately 2 mm wide and 3 mm deep. Since only one set of grooves was used at a time, the unused grooves were covered with cellophane tape to make the walls smoother. A mirror was placed next to the tank at an angle of approximately 45° so that an observer who was looking down from above could see both a top and side view of the tank. The tank and apparatus were mounted on the two-metre turntable at the Woods Hole Oceanographic Institution. The shaft of the table had been levelled to better than five seconds of arc. A 16 mm motor-driven ciné camera was rotated in synchronization with the turntable so that films could be taken of the flows in the tank with the use of small paper floats that were sprinkled on the surface of water in the tank.

For each experimental run the tank was first filled with tap water to a depth of 18·7 cm. The temperature of the water matched the temperature of the room to within 0·1 °C, to minimize convectively driven flows. A measured amount of salt was then added to the water, and mixed thoroughly in order to eliminate the slightest detectible stratification. The gate was then slid into the set of slots that were 49 cm from one end of the tank. The bottom of the gate was 10 cm above the bottom of the tank so that pressure equilibration existed. Two pieces of one-quarter inch plywood were then floated in the 49 cm long chamber, the tank was covered by a Plexiglas lid, the turntable was brought to the desired rate of rotation, and the salt water was allowed to spin up for 15 min to a state close to solid-body rotation. The preparation for the experiment was completed by slowly and carefully siphoning some coloured fresh water onto the plywood floats in the small chamber until a desired depth (2, 4 or 8 cm) of fresh water floated above the salty water. The density of the two waters was not measured directly but was estimated by means of a linear curve of density as a function of weight of salt added to the bottom water. Fractional density differences $\Delta\rho/\rho$ in the experiments were estimated to be 2·1, 3·2, 4·3, 8·7, 13·1 or $17{\cdot}5 \times 10^{-3}$. All these values are below the densities which were in the table in Hodgman (1961). The curve we used was a linear extrapolation from the one and two per cent values in the handbook. Errors are less than ten per cent, and to this accuracy, temperature and potassium permanganate have negligible effect on density.

Just before the experiment was started, the Plexiglas cover was removed from the

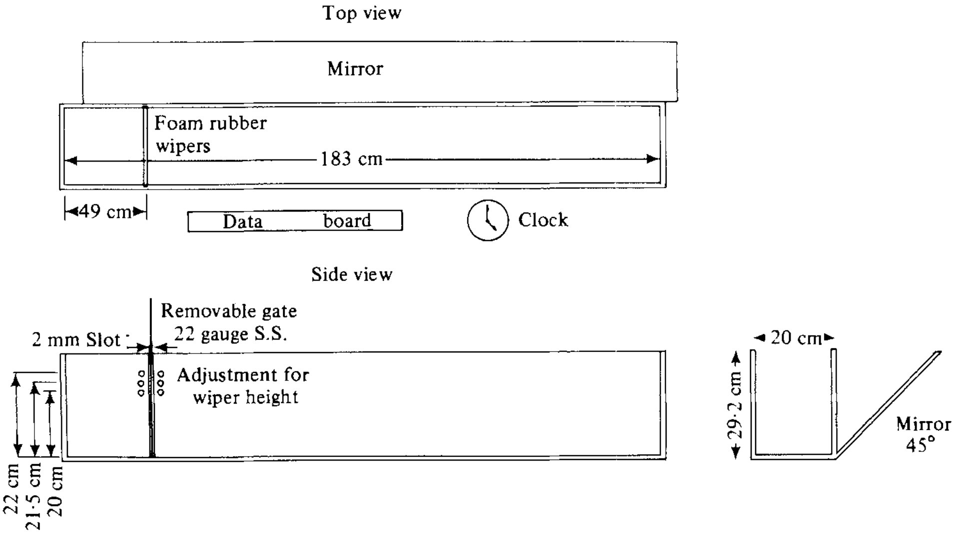

FIGURE 2. Sketch of the experimental apparatus.

tank, the ciné camera was started, and the sliding gate was carefully removed. In order to reduce the dripping effect from the emerging gate, a foam wiper was placed on each side of the guiding frame through which the gate was slid. The foam wipers were positioned so as to just contact the surface of the water after the coloured water had been put in. Use of the wipers and the guide frame in removing the gate resulted in a less-disturbed starting interface between the light and heavy fluids.

2.2. *Measurements and analysis of data*

After the gate was lifted, small paper floats were 'sprinkled' on the radially collapsing dye front in the channel, and ciné pictures were taken of the side-view mirror as well as the plan view.

The method of analysis was strongly tailored after the features of the flowing bore that were observed. The principal features of the bore (sketched in figure 3) are somewhat visible in figure 4. The nose of the bore (figure 4*a*) was not steady, but eddies peeled off the outer region and were left behind with a much slower translational velocity than the nose of the bore. On the wall immediately behind the nose was a 'neck', which was often the thinnest and shallowest portion of the laminar jet behind the nose. Although the neck was visible a sizable percentage of the viewing time, it was sometimes obscured by the edge of an eddy that had been detrained from the nose. Behind the neck were two regions. Near the wall an approximately laminar current supplied fresh fluid to the nose of the bore. This current was bordered on the outside by a region of strong cyclonic vorticity ('vortex sheet'), which separated the current from a region of eddies. These 'large-scale' eddies were complicated and turbulent in appearance. Some had been generated from the detraining process at the nose of the bore and some seem to have been detrained further upstream as illustrated more clearly in figure 4(*b*). Particles in the laminar current near the wall appeared to speed up and slow down as the eddies deformed the outer edge of the jet, but the particles in this current did not reverse direction relative to the nose, while the particles in the eddy region clearly did. There are many instances in the

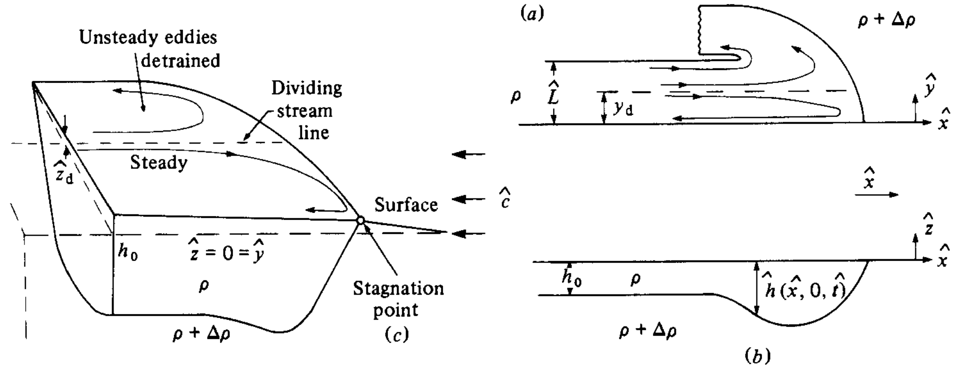

FIGURE 3. Schematic diagram of a quasi-equilibrium rotating bore far from the source region. The streamlines show the motion relative to an observer moving with the nose speed $\hat{c}$. The relative mass transport (*a*) at $\hat{x} = -\infty$ is non-zero. The detrained fraction δ of the flow reappears on the other side of the laminar vortex sheet ($\hat{y} = \hat{L}$), and is left behind as the nose propagates along the coast.

ciné films when it was difficult or even impossible to distinguish the laminar current from the eddies, but there are other instances when it was easy to distinguish between the two. In those cases the eddy activity was small outside of the laminar current, and the region separating the boundary current from the eddies had a strong shear. The continuity of this vortex sheet is visible in the ciné films, and more so to the eye while the experiment is running. We have therefore attempted to quantify the width of the boundary current by measuring the distance from the vortex sheet, when visible, to the wall.

The measuring procedure was to set up a ciné projector at a set distance from a piece of white cardboard screen. An investigator (J.W.) would sit next to the screen and look for clear instances of the vortex sheet. When one was sighted, dividers would be placed on the screen, with one point on the vortex sheet and one on the tank wall. The projector was then stopped as promptly as possible, and the distance from the span of the dividers measured. With the projector still stopped, the corresponding wall depth of the dyed fluid (in the 45° mirror) was also measured with a ruler and dividers. The time and downstream location of this measurement were recorded, as well as the nose location. This procedure was repeated in each run until measurements were taken at all positions of a clear vortex sheet. The number of samples in each run ranged from two to sixteen according to the quality and the subjective identification of a vortex sheet. We intentionally ran as many extreme values of g^* and f as possible (see table 1) in order to sample a wide variety of parameter space, so some runs are close to marginal in quality. We emphasize, however, that an unmistakable difference exists between this 'vortex sheet' and the density or dye front, aside from the fact that a precise measurement of the latter is also ambiguous and difficult.

The reason for the qualitative difference is quite clear from the observations. Dyed fluid that entered the nose (figure 3) exited in the rear and was left behind as an eddy or wave as the nose marched on. Although this was a major event for the long-time mixing of density (and also vorticity) in the boundary current, it was clearly a 'secondary' effect, and, in order to determine the primary width of the boundary current, it is quite reasonable to bias the observations towards a measurement of the shear lines. The number of 'independent' and usable measurements of $\hat{L}$ in each run

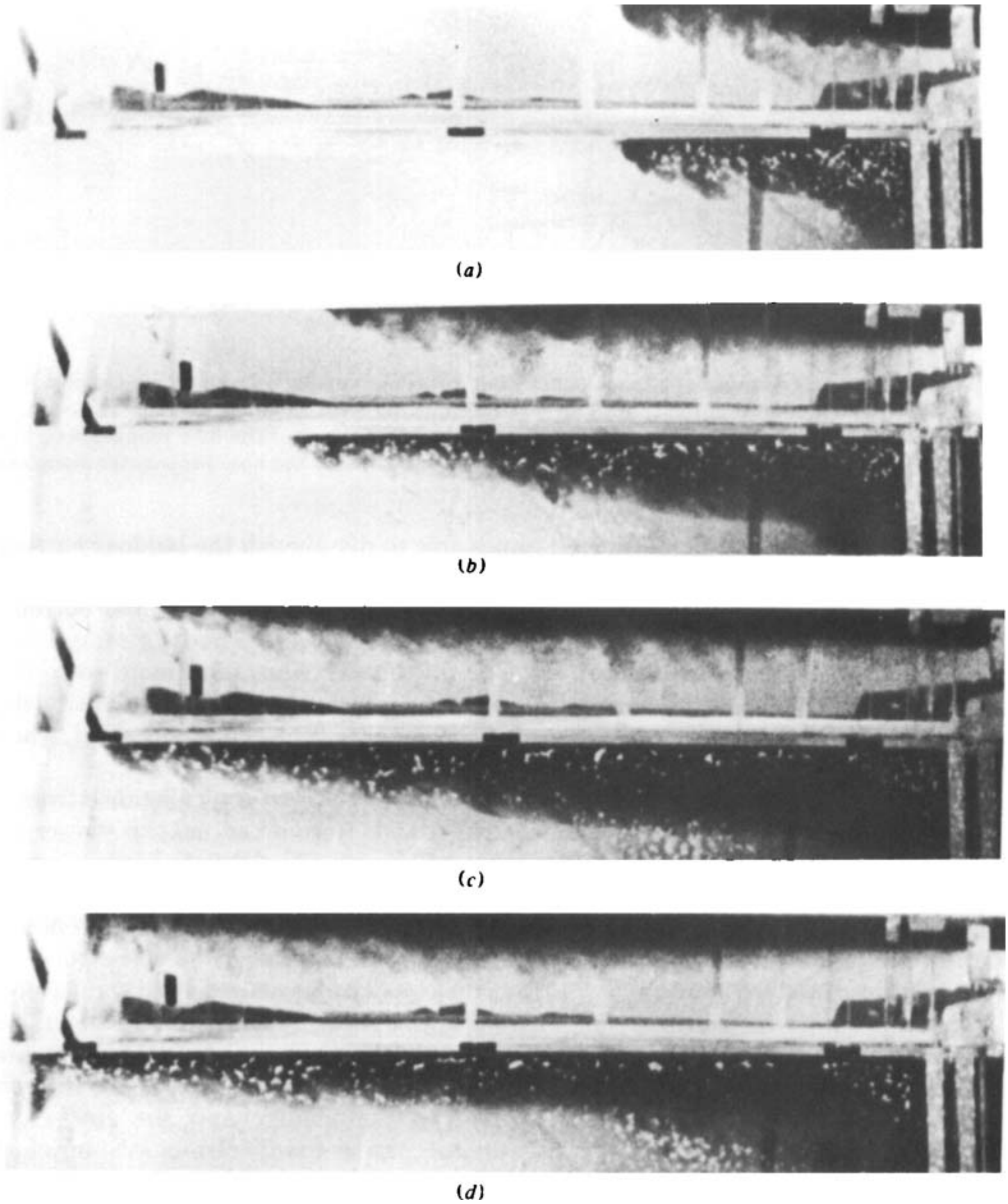

(*a*)

(*b*)

(*c*)

(*d*)

FIGURE 4 (*a–d*). For caption see facing page.

is shown by the numbers inside the circled data points (figure 5). The plotted $\hat{L}$ is the average distance from the wall of the points of maximum lateral shear in each run, and $\hat{h}$ is the average value of the corresponding wall height. The measurements of $\hat{L}$ and $\hat{h}$ were confined to a certain space–time interval that is determined by theoretical and practical considerations. Thus no measurements were taken until some time after the gate was lifted, and no measurements were taken after the nose reached the end of the tank and started to wind around the tank. No $(\hat{L}, \hat{h})$-measurements were taken in the nose of the bore, or at very large distances upstream

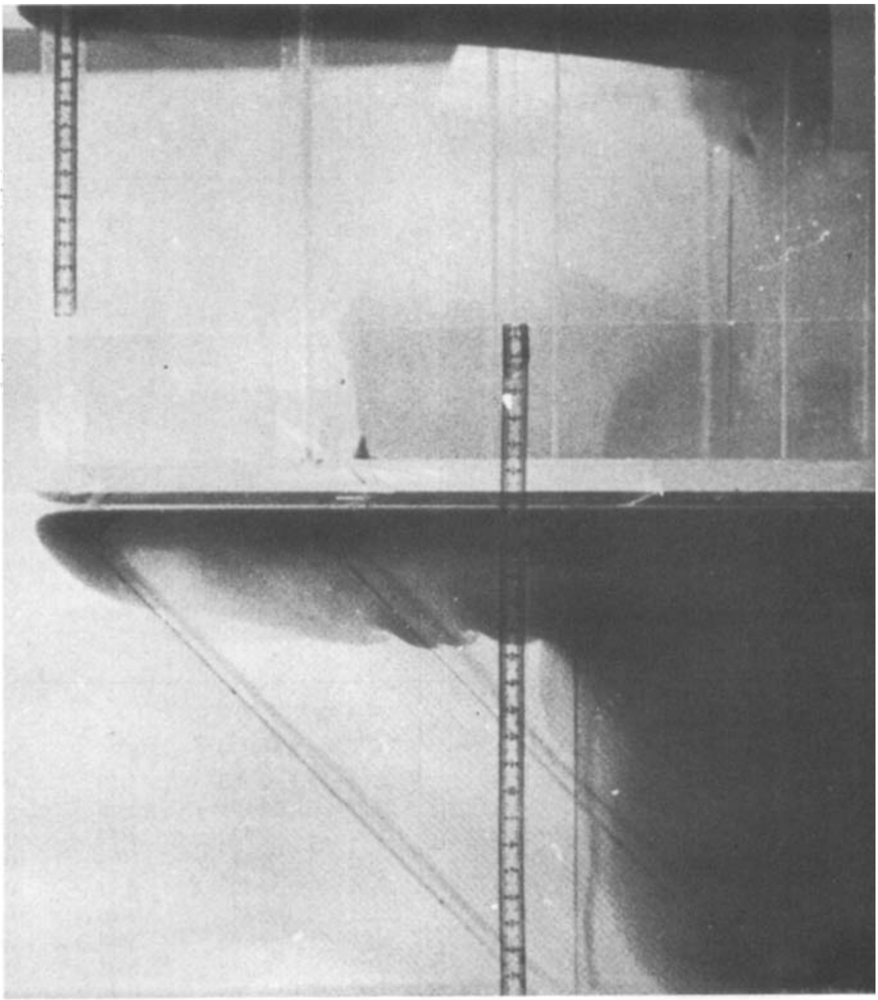

(*e*)

FIGURE 4. (*a*) A rotating density current in its early stage propagating along the right-hand wall of the tank. The image on the top is viewed through a 45° mirror and is a side view of the current with gravity downward in this figure. The image on the bottom is a plan view. The parameters are $g^* = 8{\cdot}5$, $T = 15{\cdot}4$ and $H = 8{\cdot}7$. (*b*) The same current 18 s later. The properties of the nose, such as speed, upstream width, and height, have changed little, although the eddies being shed are a little smaller. (*c*) The same current 31 s after (*a*). The current exhibits a great deal of similarity to (*b*). (*d*) After the current has hit the end of the tank, it turns the corner. The side view shows the depth of penetration of the fluid at the corner stagnation point, and illustrates that the fluid still possesses a significant amount of its original potential energy. (*e*) This intrusion (plan view) was at a relatively low Reynolds number, and the eddy that is being shed at the nose is almost laminar.

from the nose, and only a relatively small number of measurements were taken in the 'neck' behind the nose.

Conversion of the ciné-film measurements to real centimetres was determined from the image of 5 cm fiduciary marks in the side and top images. In both cases, no correction was made for parallax as the bore moved along the tank, since we estimate that the geometric corrections are smaller than the uncertainty due to the

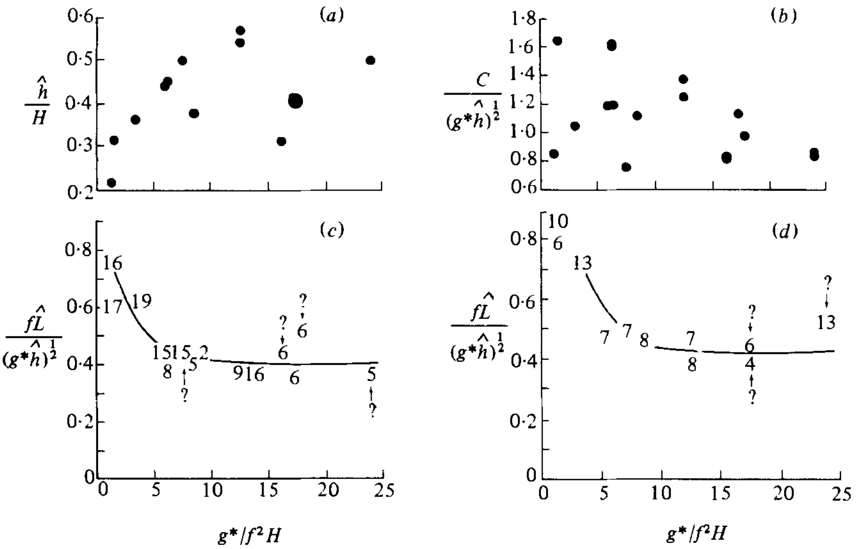

FIGURE 5. Suitable normalized values of height (*a*), bore nose velocity (*b*), and bore width for 90° gate (*c*) and 45° gate (*d*) as a function of the hydrostatic number. The numbers in (*c*) and (*d*) denote the number of observations of regions of distinct shear that went into the average.

g^* (cm/s)	$T(=4\pi/f)$ (s)	H (cm)	g^*/f^2H	$(g^*H^3)^{\frac{1}{2}}/\nu$	$f\hat{L}(g^*\hat{h})^{-\frac{1}{2}}$	$c(g^*\hat{h})^{-\frac{1}{2}}$	h_{nose}/H
17·15	14·5	4	5·84	3313	0·495	1·19	0·438
17·15	15·0	4	6·27	3313	0·494	1·19	—
12·8	20·25	4	8·5	2862	0·435	1·12	0·375
3·1	59·6	4	17·8	1408	0·52	0·98	0·400
3·1	40·6	4·2	7·68	1515	0·42	0·74	0·500
8·5	30·1	4	12·5	2332	0·37	1·25	0·571
8·5	15·4	8·7	1·57	7481	0·605	1·65	0·314
8·5	29·4	8	6·20	6597	0·382	1·64	0·450
4·2	15·3	4·6	1·24	2022	0·763	0·85	0·215
12·8	30·5	6·0	12·6	5258	0·387	1·37	0·542
2·1	60·7	3·0	16·3	753	0·435	0·82	0·318
3·1	59·3	4·0	17·25	1409	0·343	1·14	0·414
3·1	60·6	3·0	24·03	915	0·369	0·87	0·500
4·2	21·9	4·0	3·18	1640	0·632	1·04	0·357

TABLE 1. 90° Experimental parameters and results.

subjective factor entering the measurement. Data for the experiments are shown in tables 1 and 2.

The measurements of depth and width were used in the non-dimensionalized number $f\hat{L}(g^*\hat{h})^{-\frac{1}{2}}$ in the above tables, and the results were plotted as a function of g^*/f^2H in figure 5. This latter number we call a 'hydrostatic number' as it is the inverse-square ratio of the thickness H of the less-dense fluid layer in the reservoir and the Rossby radius of deformation. The reciprocal hydrostatic number is also a measure of the slope of the undisturbed front in the vertical plane sketched in figure 1. In shallow-water dynamics, and in most other large-scale geophysical problems the

g^* (cm/s^2)	$T(=4\pi/f)$ (s)	H (cm)	g^*/f^2H	$f\hat{L}(g^*\hat{h})^{-\frac{1}{2}}$
17·5	14·5	4·4	5·18	0·48
12·8	20·4	4·0	8·43	0·47
3·1	59·6	4·0	17·4	0·45
4·2	21·9	4·0	3·18	0·73
8·5	15·5	8·7	1·49	0·80
8·5	29·3	8·0	5·78	0·49
3·1	60·5	3·0	24·03	0·53
8·5	30·3	4·0	12·35	0·46
12·8	30·4	6·0	12·48	0·37
4·2	15·3	4·6	1·11	0·86
3·1	59·3	4·0	17·26	0·38

TABLE 2. 45° Experimental parameters and results.

hydrostatic number is large and irrelevant, since it disappears with the introduction of the hydrostatic assumption. This might not be true for engineering or some estuarine problems, however.

Figure 5 shows that when the hydrostatic number is above five, $f\hat{L}(g^*\hat{h})^{-\frac{1}{2}}$ is relatively constant; for the data in figure 5 and table 1 with hydrostatic number greater than five, the average value is 0·423 with a standard deviation of 0·056.

In view of the subjective and arbitrary factors in the measured width, three reproducibility tests were conducted. Experiments were performed for two initial conditions: a gate at right angles to the wall of the tank, and another at 45°. The quality of the latter experiments was somewhat lower, but it was attempted to duplicate the external parameters (g^*, H and f) as closely as possible and to compare results. Both results are shown in figure 5. For the 45° gate the average value of the width for $g^*/f^2H > 5$ is 0·453 with a standard deviation of 0·051. The most severe reproducibility test involved the use of a student to re-analyse the movies! Approximately 50 % of the data agreed with the measurements by J.W. to within 10 %. This occurred for those runs where the vortex sheets were clearly the most visible and least ambiguous. There was one period at the beginning of the test where the student was consistently lower by approximately 50 %. This occurred during one afternoon and may be due to a conservative streak during that day. The remaining 20 % were also somewhat smaller than the measurements by J.W., but appeared to be better in quality. Therefore J.W. repeated his measurements very carefully, and those data are reported here. These occurred in the experiments which were most difficult to measure denoted by question marks in figure 5.

Another check on the quality of the data was to look at the ciné films at one sitting and rate them good or marginal, based upon the clarity of the vortex sheets seen in the films. (As is often the case, the vortex sheet is easier to see in the laboratory than it is in the film because the movement of head and eyes aids the perception.) The marginal ones are labelled with a question mark in figure 5, and they only occurred when g^* was small (2·1 or 3·2 cm s^{-2}). Under the latter conditions surface tension may generate a surface 'stiffness' by creating a surface traction against convergence and divergence. It is evident that some of the marginal cases were furthest from the line.

The curves for $\hat{L}$ in figure 5 have been drawn by eye, and are slightly biased by the preceding consideration, but the asymptote at large hydrostatic number seems

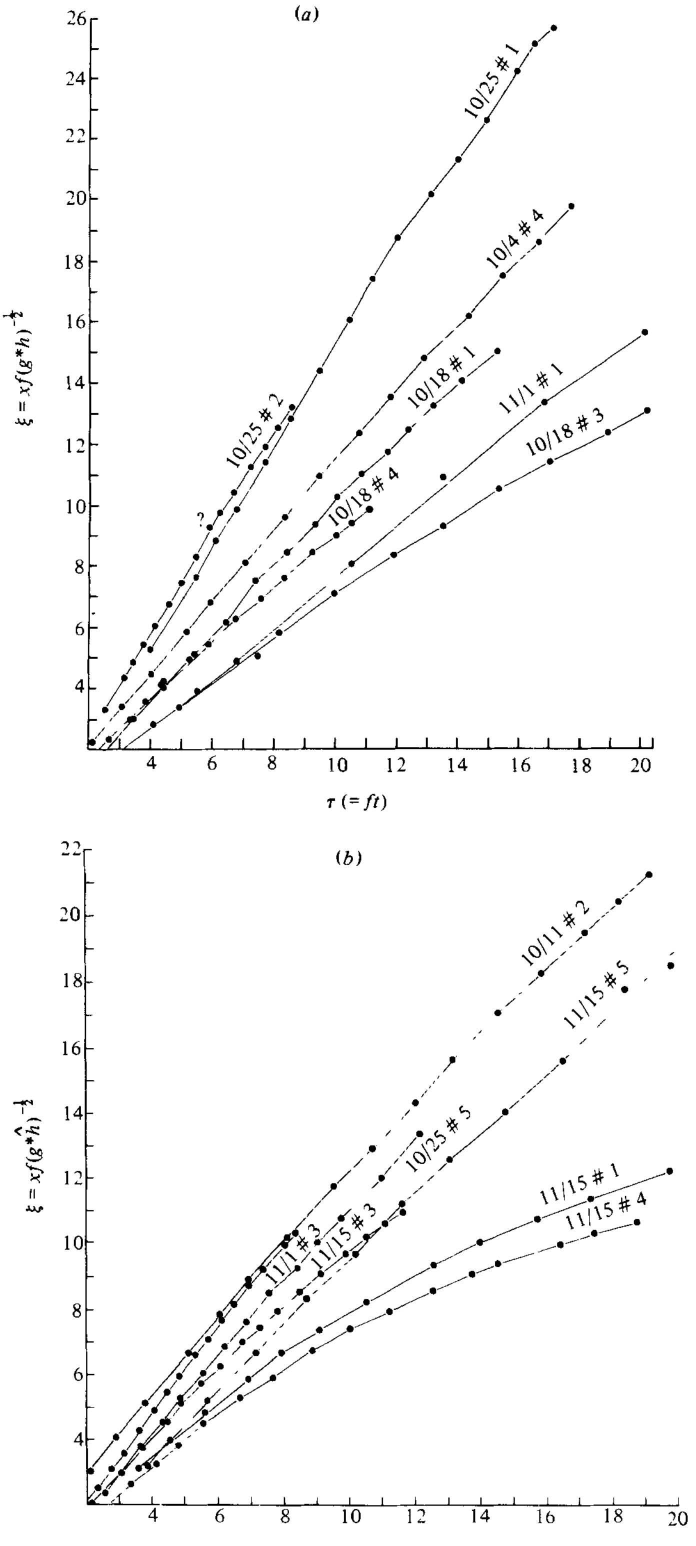

FIGURE 6. Position of the nose of the bore as a function of scaled time for the fourteen experimental runs with the 90° gate.

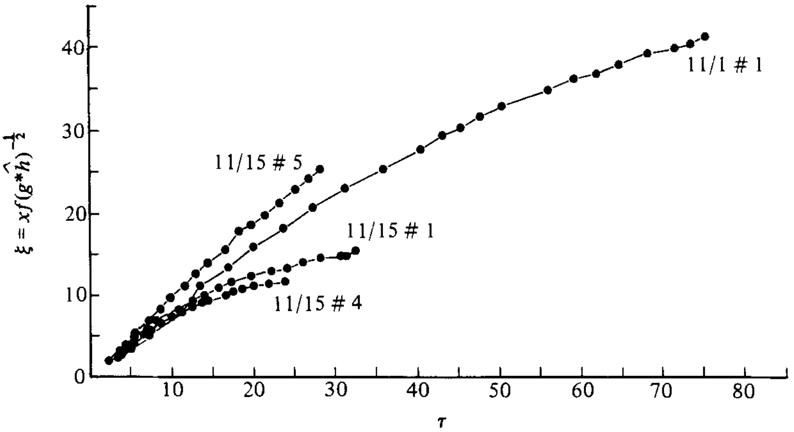

FIGURE 7. Position of the nose of the bore as a function of time for runs that lasted a large number of rotation time scales.

to be highly significant and relevant to the theory in the following sections. Thus we tentatively conclude that there is a unique width for the shear zone for the large hydrostatic number, with

$$\frac{f\hat{L}}{(g^*\hat{h})^{\frac{1}{2}}} = 0{\cdot}423 \pm 0{\cdot}056 \tag{2.1}$$

for the 90° barrier, and

$$\frac{f\hat{L}}{(g^*\hat{h})^{\frac{1}{2}}} = 0{\cdot}453 \pm 0{\cdot}051 \tag{2.2}$$

for the 45° barrier.

It is conceivable, however, that there may be not *one* curve, but a whole band of curves, i.e. the jet width may not be unique but may depend on other factors which are not within our control – such as the instability waves that form on the front in the reservoir when the barrier is removed.

This point of view is also suggested by the measurements of bore speed (figures 6*a*, *b*), which were only taken for the runs with a gate at 90°. The ordinate is the non-dimensional displacement of the nose bore from the dam, the abscissa is the non-dimensional time, and the points are the observations for each run. The identifying date and run numbers are also indicated. The curves drawn through these points have smoothed out some small variations in bore speed that may be real. A decrease of slope with increasing time can be clearly seen in some of the runs, and after very large times (figure 7) some of the noses stagnate and curve away from the wall forming a large gyre! The lack of 'similarity' of the curves is apparent. For each curve the extrapolated (small time) tangent has been drawn, and the corresponding non-dimensional speed $\hat{c}(g^*\hat{h})^{-\frac{1}{2}}$ computed. For figure 6(*a*) the mean speed is $c = 1{\cdot}09$, and for figure 6(*b*) it is $c = 1{\cdot}16$. In both figures the variation of $\hat{c}$ is real, but no correlation with g^*/f^2H has been found. Figure 8, however, indicates some systematic variation of $\hat{c}$ with the product of the velocity scale $(g^*H)^{\frac{1}{2}}$ and the depth scale H; and therefore the results (figure 8) have been plotted as a function of the overall Reynolds number $H(g^*H)^{\frac{1}{2}}\nu^{-1}$, even though the viscosity was not varied in the experiment. The implicit assumption here is not unreasonable, because Simpson & Britter (1979) observe that the nose speed in a non-rotating density current depends on Reynolds number when the latter is less than 10^3. The *dynamically* significant

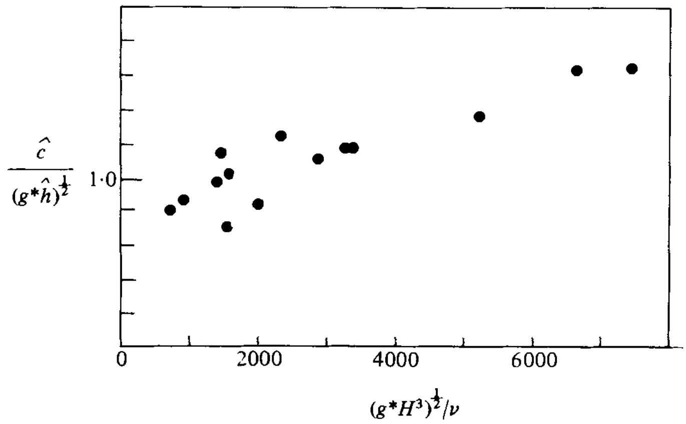

FIGURE 8. Scaled velocity as a function of the overall Reynolds number.

Reynolds number may be a proportionally smaller value for three reasons: (i) the depth of the jet is less than upstream height H (figure 5); (ii) the depth of the jet varies across the stream and goes to zero; and (iii) the depth of the nose is small and goes to zero at the leading edge. At large Reynolds number (> 4000) the envelope of the data tends to $c = 1{\cdot}56$ with a standard deviation of $0{\cdot}05$. At smaller Reynolds number the phase speed is approximately 20 % less. It is plausible that the systematic effect of the nose viscosity on the upstream width (figure 5*c*, *d*) is less than or equal to this 20 %.

3. A quasi-steady theory for a rotating density current

Figure 3 is a schematic diagram of the nose of the boundary intrusion as it is flowing along in a statistically steady state. The streamlines are drawn relative to an observer who moves with speed $\hat{c}$ of the nose of the intrusion (and in this frame of reference the nose is thus a stagnation point).

Under ideal conditions one would like to consider the light fluid to be separated from the heavy fluid by an interfacial surface that intersects the free surface ($\hat{z} = 0$) at the 'front'; the latter being a free streamline and a vortex sheet. This idealization differs somewhat from a more realistic sketch (figure 3) of our experimental observations, which shows part of the boundary flow entering the nose region and being left behind (*detrained*) as it folds the front backwards. The sketch in figure 3 illustrates the continuous nature of the fields and replaces the vortex discontinuity of the free streamline by a strong maximum-shear line (at $\hat{L}$) lying outside the dividing streamline. The width $\hat{L}$ that was actually measured in the experiments corresponds to this strong maximum-shear line. Another dynamically significant width is the dividing streamline (figures 3*a*, *c*), located at distance $\hat{y}_{\mathrm{d}}$ from the wall. The distance $\hat{y}_{\mathrm{d}}$ is defined such that the mass transport relative to the nose vanishes in the interval $\hat{y} = 0$ to $\hat{y} = \hat{y}_{\mathrm{d}}$, i.e.

$$\int_0^{\hat{y}_{\mathrm{d}}} (\hat{u}-\hat{c})\,\hat{h}\,d\hat{y} = 0, \tag{3.1}$$

where $\hat{u}$ is the longshore ($\hat{x}$) component of the vector velocity $\hat{\mathbf{V}}$ in the non-translating (f-frame) system, and $\hat{h}$ is the local layer thickness of a two-layer model. All the quantities in (3.1) are evaluated far upstream from the nose ($\hat{x} = -\infty$), in a region

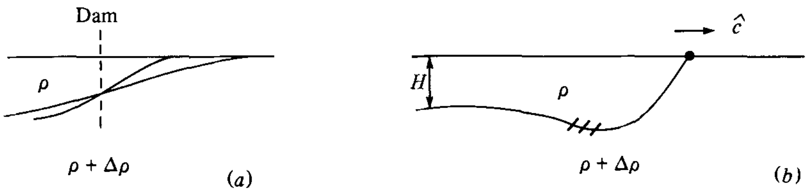

FIGURE 9. (*a*) For a non-rotating dam-break problem, the initial-value solution gives a thinning 'wedge' for the shape of the intruding light water of density ρ. (*b*) The non-rotating bore in the quasi-equilibrium Kármán–Benjamin theory.

$\hat{y} < \hat{y}_{\mathrm{d}}$ where our observations indicate the flow to be approximately steady and laminar. On the other side of the dividing streamline, however, our observations indicate a much more unsteady and non-laminar flow. Thus a conservative Bernoulli function exists for the region inside the dividing streamline, and this function is found by transforming the equations of motion from the f-frame to a frame that translates with relative speed $\hat{c}$.

If $\hat{p}$ is the pressure, and if $\hat{z}$ is the height of a point above a level surface in the f-frame, then the $\hat{c}$-frame velocity $\hat{\mathbf{V}}_c$ satisfies

$$d\hat{\mathbf{V}}_c/d\hat{t}+f\mathbf{k}\times\hat{\mathbf{V}}_c+f\mathbf{k}\times\hat{\mathbf{c}} = -\rho^{-1}\nabla\hat{p}-g\nabla\hat{z}.$$

A Bernouli equation may be formed from this by taking the scalar product with the solinoidal $\hat{\mathbf{V}}_c$ and writing the result in the form

$$\frac{1}{2}\frac{d\hat{\mathbf{V}}_c^2}{d\hat{t}}+f\hat{c}\frac{d\hat{y}}{d\hat{t}} = -\rho^{-1}\frac{d\hat{p}}{d\hat{t}}+\rho^{-1}\frac{\partial\hat{p}}{\partial\hat{t}}-\frac{g\,d\hat{z}}{d\hat{t}}.$$

If the motion on any free-surface (p = constant) streamline is steady in the translating frame, then the Bernoulli function

$$B = \tfrac{1}{2}\hat{\mathbf{V}}_c^2+f\hat{c}\hat{y}+g\hat{z} \tag{3.2}$$

is invariant, and this assumption will be made for certain regions in the flow.

Reference is first made to Benjamin's (1968) selective use of the Bernoulli invariant for the problem (figure 9) of a non-rotating density intrusion. Von Kármán (1940) proposed a completely steady solution, but this does not exist. The main region of unsteadiness is located in the hatched region of figure 9, which region is somewhat analogous to the unsteady lateral front in our problem. We shall, therefore, follow Benjamin by assuming invariance of (3.2) in regions removed from the mixing sites.

Steady relative motion is now assumed on the free-surface streamlines located at $\hat{y} = 0$, i.e. along the two streamlines passing through the stagnation point. At $\hat{x} = \infty$ in the heavy-fluid region, the velocity $\hat{\mathbf{V}}_c$ relative to the nose is given by $\hat{u}_c = -\hat{c}$, and the Bernoulli invariant then gives:

$$\tfrac{1}{2}\hat{c}^2 = g\hat{z}_{\mathrm{s}}, \tag{3.3}$$

where $\hat{z}_{\mathrm{s}}$ is the geopotential height of the stagnation point. The other streamline lying in the light-fluid region yields:

$$\tfrac{1}{2}(\hat{u}_{-\infty}-\hat{c})^2+g\,\hat{z}_{-\infty} = g\hat{z}_{\mathrm{s}}, \tag{3.4}$$

where $\hat{u}_{-\infty}$ is the velocity ($\hat{\mathbf{V}}$) and $\hat{z}_{-\infty}$ is the geopotential far upstream from the nose.

The elimination of $\hat{z}_s$ gives

$$\tfrac{1}{2}(\hat{u}_{-\infty}-\hat{c})^2+g\hat{z}_{-\infty}=\tfrac{1}{2}\hat{c}^2. \tag{3.5}$$

Since the geopotential height of the upstream free surface on the wall is related to the layer thickness $\hat{h}_0$ by the hydrostatic consideration, i.e. $(\rho+\Delta\rho)\,\hat{z}_{-\infty}=\Delta\rho\hat{h}_0$, one can rewrite (3.5) as

$$\hat{c}=\tfrac{1}{2}\hat{u}_{-\infty}+\frac{g^*\hat{h}_0}{\hat{u}_{-\infty}}, \tag{3.6}$$

where $g^*=g\Delta\rho/\rho$.

In the non-rotating theory with no detrainment $\hat{u}_{-\infty}$ is a constant equal to $\hat{c}$, and the use of this gives $\hat{c}=(2g^*\hat{h}_0)^{\frac{1}{2}}$. Although a mass flux relative to the nose is always observed (Britter & Simpson 1978), the quantitative effect on $\hat{c}$ of this detrainment is small (in a limiting case), presumably because of the strong opposition of gravitational stability.

But in our problem (figure 3) *lateral* detrainment can occur without great gravitational opposition, and the effect is indeed most striking in our experiments. We will therefore reject the assumption that the upstream volume transport of the intrusion (relative to the nose) is zero, and the finite ratio of this transport to the absolute transport, i.e.

$$\delta\equiv\frac{\int_0^{\hat{L}}(\hat{u}-\hat{c})\,\hat{h}(\hat{y})\,d\hat{y}}{\int_0^{\hat{L}}\hat{u}\hat{h}\,d\hat{y}}\quad(\text{at }\hat{x}=-\infty). \tag{3.7}$$

will be called the detrainment coefficient. Furthermore, $\hat{u}(-\infty,\hat{y})$ is not independent of $\hat{y}$, and therefore additional information is required to determine the wall velocity $\hat{u}_{-\infty}=\hat{u}(-\infty,0)$.

The reader may want to turn to appendix A at this point, where Bernoulli invariance is also applied to the dividing streamline, and where a simple argument leads to an upper bound on $\hat{y}_d$. The following argument, on the other hand, claims to give a sharper prediction of the width of the current to use in connection with (3.6).

4. Intrusion of finite potential vorticity

What are the dynamical factors that determine $\hat{L}$, $\hat{c}$, $\hat{\delta}$? As a start, we are obliged to introduce rather drastic assumptions, one of which, (see §4.3), involves a recognition that the experiment involves a 'self-limiting' process in which certain factors ($\hat{L}$, $\hat{c}$, $\hat{\delta}$) are largely independent of the initial conditions. Another assumption is the use of the shallow-water equations

$$d\hat{\mathbf{V}}/d\hat{t}+f\mathbf{k}\times\hat{\mathbf{V}}=-g^*\nabla\hat{h}, \tag{4.1}$$

$$\partial\hat{h}/\partial\hat{t}+\nabla\cdot\hat{\mathbf{V}}\hat{h}=0 \tag{4.2}$$

as the starting point. These apply to two layers (figure 1) of slightly different ($\Delta\rho$) density, the lower layer being relatively thick and passive. The upper layer has thickness $\hat{h}(\hat{x},\hat{y},\hat{t})$ and velocity $\hat{\mathbf{V}}=(\hat{u},\hat{v})$. There is a vertical coast at $\hat{y}=0$ so that the transverse velocity is $\hat{v}(\hat{x},0,\hat{t})=0$, and there is a free streamline at $\hat{y}=\hat{L}(\hat{x},\hat{t})$ so that $\hat{h}(\hat{x},\hat{L}(\hat{x},\hat{t}),\hat{t})=0$. The neglect of the friction forces in (4.1) must be kept in mind, especially when one considers explicitly the nose region.

Relevant initial-value solutions of (4.1)–(4.2) are still difficult to obtain, and we shall therefore retreat still further to a generalization of Stern's theory for the evolution of long waves on a uniform potential vorticity current. Plausible similarity assumptions (cf. (4.29) and the last paragraph in §4) will be made which relate the evolution of the long-wave solution to a corresponding state of the experiment.

4.1. *Long-wave equations for uniform potential vorticity*

Let us first write (4.1) in the alternative form

$$\partial \hat{\mathbf{V}}/\partial \hat{t} + (f+\hat{\zeta})\,\mathbf{k}\times\hat{\mathbf{V}} = -\nabla(g^*\hat{h} + \tfrac{1}{2}\hat{\mathbf{V}}^2), \tag{4.3}$$

$$\hat{\zeta} = k\cdot\nabla\times\hat{\mathbf{V}}, \tag{4.4}$$

and the conservation of potential vorticity $(f+\hat{\zeta})/\hat{h}$ is also implied. Therefore, if the initial state has uniform potential vorticity $f/\hat{H}$, where $\hat{H}$ is the uniform initial vertical thickness, then

$$\frac{f+\hat{\zeta}}{\hat{h}} = \frac{f}{\hat{H}} \tag{4.5}$$

at all subsequent times. The component of $\hat{\mathbf{V}}$ parallel to the coast is denoted by $\hat{u}$, the $\hat{y}$-component is denoted by $\hat{v}$, and the foregoing equations are made non-dimensional by the transformations

$$\left.\begin{array}{l} \hat{h} = h_0 h(x,y,t), \quad \hat{y} = (g^*h_0)^{\frac{1}{2}} f^{-1} y, \quad \hat{x} = \epsilon^{-1}(g^*h_0)^{\frac{1}{2}} f^{-1} x, \\ \hat{u} = (g^*h_0)^{\frac{1}{2}} u, \quad \hat{v} = \epsilon (g^*h_0)^{\frac{1}{2}} v, \quad \hat{t} = \epsilon^{-1} f^{-1} t, (4.6) \\ \hat{H} = h_0 H, \quad \hat{L} = (g^*h_0)^{\frac{1}{2}} f^{-1} L(x,t), \quad \hat{h}(\hat{x},\hat{L},\hat{t}) = 0; \end{array}\right\} \tag{4.6}$$

where h_0 is a given vertical depth scale, and ϵ is the scale value of cross-stream/downstream velocities. In figure 3(*b*), and in that which follows, h_0 is conveniently taken as the wall height of the intrusion far upstream in the laminar portion of the coastal current, and from geostrophy it follows that $g^*h_0^2/2f$ equals the volume flux.

When the non-dimensional equations are written in Cartesian form, and when the long-wave ($\epsilon \rightarrow 0$) limit is taken, the result is

$$\frac{\partial u}{\partial t} - \left(1 - \frac{\partial u}{\partial y}\right)v + \frac{\partial}{\partial x}(h + \tfrac{1}{2}u^2) = 0, \tag{4.7}$$

$$u = -\frac{\partial h}{\partial y}, \tag{4.8}$$

$$\frac{\partial h}{\partial t} + \frac{\partial hu}{\partial x} + \frac{\partial hv}{\partial y} = 0, \tag{4.9}$$

$$1 - \frac{\partial u}{\partial y} = \frac{h}{H}. \tag{4.10}$$

It is easy to show (by taking the y-derivative of (4.7)) that (4.7) is satisfied at all y if it is satisfied at any one particular y, and if (4.8)–(4.10) are satisfied at all y.

Equations (4.8) and (4.10) give an ordinary differential equation for h, and if $U(x, t)$ denotes the value of u on $y = L$ (where $h = 0$) then the solution is

$$h(x,y,t) = H\left[1 - \cosh\frac{L-y}{H^{\frac{1}{2}}}\right] + H^{\frac{1}{2}} U \sinh\frac{L-y}{H^{\frac{1}{2}}}, \tag{4.11}$$

$$u(x,y,t) = -H^{\frac{1}{2}}\sinh\frac{L-y}{H^{\frac{1}{2}}} + U\cosh\frac{L-y}{H^{\frac{1}{2}}}. \tag{4.12}$$

The zero-potential-vorticity limit $H^{-1} \to 0$ yields Stern's (1980) results with $h = U(L-y)-\frac{1}{2}(L-y)^2$ and $u = U-L+y$.

4.2. *Time-dependent equations*

When profiles of u and h are substituted in (4.7), and the result evaluated at the particular $y = L$ (where $1-\partial u/\partial y = 0$), we get

$$\frac{\partial U}{\partial t}+U\frac{\partial U}{\partial x}-\frac{\partial L}{\partial t}=0. \tag{4.13}$$

Note that v appears only in (4.7), and its coupling with (U, L) only appears via the boundary conditions, or via the integrated version of (4.9), viz

$$\frac{\partial}{\partial t}\int_0^{L(x,t)} h\,dy+\frac{\partial}{\partial x}\int_0^{L(x,t)} uh\,dy = 0. \tag{4.14}$$

The substitution of (4.11) and (4.12) in this, and the simplification of the result using (4.13), yields

$$\begin{aligned}0 &= \left(UH^{-1}\sinh\frac{L}{H^{\frac{1}{2}}}\right)\frac{\partial L}{\partial t}\\ &+\left[UH^{-\frac{1}{2}}\sinh\frac{L}{H^{\frac{1}{2}}}-\cosh\frac{L}{H^{\frac{1}{2}}}+1\right]\left[UH^{-\frac{1}{2}}\cosh\frac{L}{H^{\frac{1}{2}}}-\sinh\frac{L}{H^{\frac{1}{2}}}\right]\frac{\partial L}{\partial x}\\ &+\left[UH^{-\frac{1}{2}}\cosh\frac{L}{H^{\frac{1}{2}}}-\sinh\frac{L}{H^{\frac{1}{2}}}\right]\left[\cosh\frac{L}{H^{\frac{1}{2}}}-1\right]\frac{\partial U}{\partial x},\end{aligned} \tag{4.15}$$

which together with (4.13) form a complete set of quasi-linear hyperbolic equations for the position of the front $L(x, t)$ and the velocity $U(x, t)$ along that free streamline.

The thickness of the fluid on the wall as obtained from (4.11) is

$$h(x,o,t) = H\left[1-\cosh\frac{L}{H^{\frac{1}{2}}}\right]+H^{\frac{1}{2}}U\sinh\frac{L}{H^{\frac{1}{2}}}, \tag{4.16}$$

and by using our normalizing condition $h(-\infty, 0, t) = 1$ we get the boundary condition for the upstream state section (curve *PWQ* in figure 10):

$$1 = H\left[1-\cosh\frac{L}{H^{\frac{1}{2}}}\right]+H^{\frac{1}{2}}U\sinh\frac{L}{H^{\frac{1}{2}}} \quad \text{at} \quad x=-\infty. \tag{4.17}$$

The non-dimensional H is inversely proportional to the potential vorticity, and the simple case of zero potential vorticity may be obtained from (4.15) and (4.17) by expanding the hyperbolic functions in an $L/H^{\frac{1}{2}}$ power series. By neglecting small terms of order $L/H^{\frac{1}{2}}$ we then get

$$U\frac{\partial L}{\partial t}+(U-\tfrac{1}{2}L)(U-L)\frac{\partial L}{\partial x}+\tfrac{1}{2}L(U-L)\frac{\partial U}{\partial x}=0, \tag{4.18}$$

$$1 = L(U-\tfrac{1}{2}L) \quad \text{at} \quad x=-\infty. \tag{4.19}$$

4.3. *Similarity solutions*

There are no solutions of (4.13) that preserve their form, and the 'simplest' solutions are those in which the functional relations between $L(x, t)$, $U(x, t)$, $h(x, 0, t)$ are *independent of time* and position x. (We also note that the experimental relation between $\hat{L}$ and $\hat{h}$ is 'universal'.) Therefore, we now look for solutions such that U is some (unknown) function of $L(x, t)$ *alone*, i.e.

$$U = U(L), \tag{4.20}$$

$$\frac{\partial U}{\partial t} = U'(L)\frac{\partial L}{\partial t}, \tag{4.21}$$

$$\frac{\partial U}{\partial x} = U'(L)\frac{\partial L}{\partial x}. \tag{4.22}$$

Upon substituting this in (4.13) and (4.15) we obtain two simultaneous quasilinear equations for $(\partial L/\partial t, \partial L/\partial x)$, the first of which is

$$\frac{\partial L}{\partial t}+\frac{UU'(L)}{U'(L)-1}\frac{\partial L}{\partial x} = 0. \tag{4.23}$$

This implies that L (and U and $h(x, 0, t,)$) is constant relative to an observer moving with the local propagation speed

$$\frac{dx}{dt} = \frac{U}{1-1/U'(L)}. \tag{4.24}$$

When (4.20) is used in (4.15) we obtain a second quasi-linear equation for $\partial L/\partial t$ and $\partial L/\partial x$. Elimination of these two derivatives from the two simultaneous equations gives a quadratic equation for U'. After using some hyperbolic trigonometry to solve for $1/(U'-1)$, the roots of this quadratic can be expressed as

$$\frac{dU}{dL} = 1-\frac{(2U/H^{\frac{1}{2}})\cosh(L/2H^{\frac{1}{2}})}{a\pm(a^2+b)^{\frac{1}{2}}}, \tag{4.25}$$

$$a = \sinh(L/H^{\frac{1}{2}})\left[\cosh\frac{L}{2H^{\frac{1}{2}}}-\frac{U}{H^{\frac{1}{2}}}\sinh\frac{L}{2H^{\frac{1}{2}}}\right], \tag{4.26}$$

$$b = 2\sinh(L/H^{\frac{1}{2}})\left[\frac{U}{H^{\frac{1}{2}}}\cosh\frac{L}{H^{\frac{1}{2}}}-\sinh\frac{L}{H^{\frac{1}{2}}}\right]. \tag{4.27}$$

Equation (4.25) gives two (±) intersecting families of curves in the (U, L)-plane, and the intrusive solutions of interest pass through the nose point $L = 0$. The two families are given in figure 10 for uniform potential vorticity $H = 2$, and comparison with the zero-potential-vorticity curves (figure 11) shows that there is not much difference in the vicinity of $L = 0$.

Corresponding values of L, U far upstream must correspond to one of the points (say P) lying on the dashed auxiliary curve in figures 10 and 11. Through this point P, pass two (±) solution (4.25) curves, one of which represents a 'wedge' and the other a 'bore' intrusion (Stern 1980). A wedge solution $\oplus$ passing through P has a local propagation speed that increases towards the nose, so that an observer moving with the nose sees the wedge get thinner with time until frictional forces eventually become dominant in the nose region and slow the nose down. Thus all the 'wedges' have a divergent energy flux in the nose region, and these solutions are apparently irrelevant for the model we seek. The $\ominus$ solution (curve PS), on the other hand, can be shown (see Stern 1980) to have a local propagation speed that decreases with L, and the nose of this *bore*-like intrusion advances slower than the rear. Thus an observer sees the front steepen with time, whereupon the short-wave terms neglected in this

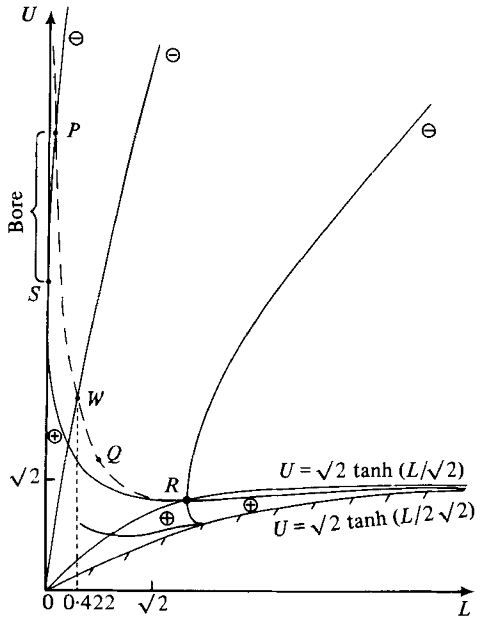

FIGURE 10. The trajectories of solutions in (U, L)-space for non-dimensional potential vorticity = 2. The limiting bore solution corresponds to the line OW and the long-dashed line corresponds to the upstream condition (4.17), which any solution must lie on.

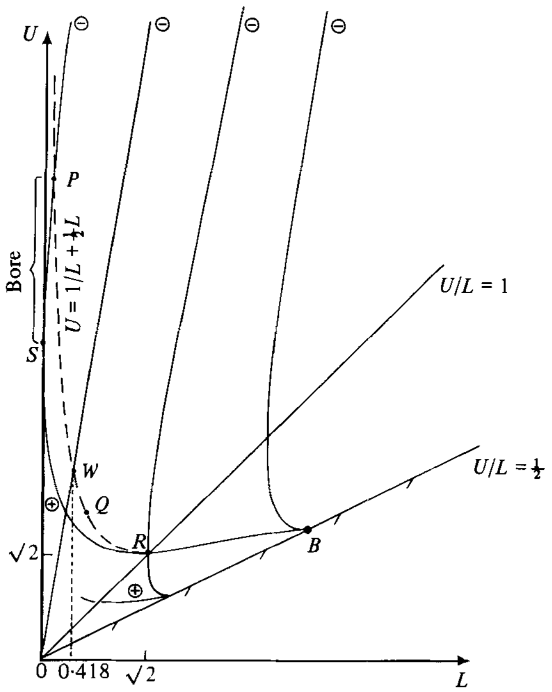

FIGURE 11. The trajectories of the solutions in (U, L)-space for zero potential vorticity.

theory become important and the 'shock' modifies the nose. Although these solutions might be relevant, we note that there is an entire family of bore solutions, corresponding to all the P-type points, and further specification is necessary.

Consider the nose region ($L = 0$) of the current, and replace the hyperbolic functions in (4.25)–(4.27) by the leading terms in a small-L expansion. The result

$$\frac{dU}{dL} = 1 - \frac{2U}{L \pm [L^2 + 2L(U-L)]^{\frac{1}{2}}}, \tag{4.28}$$

is valid for small L and all H. This relation also holds for all L when $H^{-1} \rightarrow 0$. The bore solutions are obtained by using the $-$ sign.

Equation (4.28) is infinite at $L = 0$ if $U(0)$ is finite, so that the frontal slope

$$\left.\frac{\partial L}{\partial x}\right|_{L=0} = (U'(L))^{-1} \left.\frac{\partial U}{\partial x}\right|_{L=0},$$

will vanish if $U(0) > 0$. Under these 'unrealistic' conditions, a thin nose ($\partial L/\partial x = 0$) exists at all times at $L = 0$ and, furthermore, the shock which will occur for this solution will be located *behind* the nose. The only exception occurs for the bore solution satisfying the end condition

$$U(0) = 0, \tag{4.29}$$

for then (4.28) is finite at $L = 0$. $\partial L/\partial x$ can then be finite, and $\partial L/\partial x = \infty$ can occur first at the nose. This (4.29) 'limiting bore' also has the property that its upstream width is maximal among all the intrusions that propagate as a bore. Initial states with a greater width have to adjust so that a thinner portion propagates down the coast, leaving the thicker portions behind. Further discussion of (4.29) appears in §6.

The maximum width of this limiting bore is found by integrating (4.25) with the $-$ sign:

$$\frac{dU}{dL} = 1 - \frac{(2U/H^{\frac{1}{2}})\cosh(L/2H^{\frac{1}{2}})}{a - (a^2+b)^{\frac{1}{2}}}, \tag{4.30}$$

and by using the boundary condition $U(0) = 0$. The resulting curve OW is extended until it intersects the upstream state curve at point W (figure 10).

For zero potential vorticity, Stern (1980) found that the abscissa of the latter point W is (figure 11)

$$L = 0{\cdot}418 \quad \text{for} \quad x = -\infty \tag{4.31a}$$

For finite H (4.30) was integrated by a Runge–Kutta scheme, and the result for $H = 2$ is the curve OW in figure 10. The upstream state curve (4.17) is RQW, and the point of intersection W corresponds to $L = 0{\cdot}422$. A number of values of H were taken in the range $1 < H < \infty$ and the computed L lies in the range

$$0{\cdot}418 < L(-\infty) < 0{\cdot}426. \tag{4.31b}$$

Thus we conclude that the *limiting bore* width $L \simeq 0{\cdot}42$ is essentially independent of potential vorticity.

The foregoing long-wave theory is obviously not uniformly valid, and it will fail when the first shock forms (at the nose). At that time it is reasonable to suppose that the short-wave theory ((4.1) and (4.2)) will modify the entire nose region and accelerate the nose. But it is reasonable to assume that there will be no modification upstream. This means that the value of L in the latter regions will equal the long-wave-theory result even though the nose is more drastically modified. This assumption is testable in principle by integrating (4.1) and (4.2) numerically. The non-limiting bores ($U'(0) = \infty$), on the other hand, will break first behind the nose and will probably evolve into a more complicated structure (e.g. separated flow).

5. Quasi-steady nose speed and detrainment coefficients

The limiting value of the nose speed (in the post-steepening phase mentioned above) must be consistent with the upstream mass flow, and with the Bernoulli condition, i.e. (3.6) and (3.7). The $\hat{u}(y)$, $\hat{h}(y)$ appearing in the latter are to be evaluated far upstream, and, according to the main assumption at the end of §4.3 are given by the long-wave theory.

The calculations are given first for zero potential vorticity, ($H^{-1} \rightarrow 0$), in which case (4.11), (4.12) and (4.17) reduce to

$$u = U-L+y, \quad h = U(L-y) - \tfrac{1}{2}(L-y)^2, \quad 1 = UL - \tfrac{1}{2}L^2 \quad \text{at} \quad x = -\infty,$$

and from these we get

$$\int_0^L hu\,dy = \tfrac{1}{2}h^2(0) = \tfrac{1}{2} \quad \text{at} \quad x = -\infty,$$

$$\int_0^L h\,dy = \tfrac{1}{2}UL^2 - \tfrac{1}{6}L^3 = \tfrac{1}{2}L + \tfrac{1}{12}L^3 \quad \text{at} \quad x = -\infty.$$

The wall velocity is then $u(-\infty, 0) = 1/L - \frac{1}{2}L$. Since $L = 0{\cdot}418$ (4.31*a*), (3.6) and (3.7) yield

$$c = 1{\cdot}546, \tag{5.1}$$

$$\delta = 0{\cdot}332. \tag{5.2}$$

For finite potential vorticity, one has

$$u = \frac{(1-H)\cosh L/H^{\frac{1}{2}} + H}{H^{\frac{1}{2}}\sinh L/H^{\frac{1}{2}}} \quad \text{at} \quad x = -\infty, \quad y = 0, \tag{5.3}$$

$$\int_0^L hu\,dy = \tfrac{1}{2}h^2(0) = \tfrac{1}{2} \quad \text{at} \quad x = -\infty, \tag{5.4}$$

$$\int_0^L h\,dy = H\left[L + \frac{1-2H}{H^{\frac{1}{2}}\sinh L/H^{\frac{1}{2}}}\left(\cosh\frac{L}{H^{\frac{1}{2}}} - 1\right)\right] \quad \text{at} \quad x = -\infty. \tag{5.5}$$

When $H = 2$, we have found that $L = 0{\cdot}42$ (figure 10), and the values of (3.6) and (3.7) are then computed to be $c = 1{\cdot}57$ and $\delta = 0{\cdot}32$. For the whole range $1 < H < \infty$, the values of (c, δ) do not differ by more than 3 % from the above values. Thus we conclude that the nose speed, detrainment coefficient and boundary-current width are essentially independent of the potential vorticity for a given volume transport (i.e. h_0).

We have also investigated (appendix C) the effect of a finite bottom layer, and found that this increases the range of widths of the boundary current to

$$0{\cdot}413 \leqslant L(-\infty) \leqslant 0{\cdot}516,$$

and $L(-\infty) = 0{\cdot}43$ when the total depth is twice the upper layer depth (h_0) and when $H = 2$. Under these conditions $C = 1{\cdot}56$ and $\delta = 0{\cdot}34$. Thus we conclude that the boundary current width, speed c, and detrainment coefficient are insensitive to the lower-layer depth as well as to the upper-layer potential vorticity.

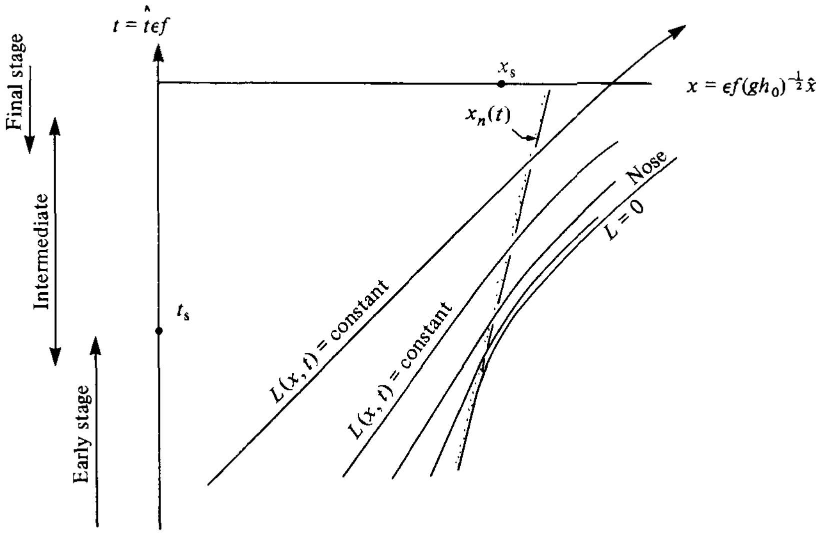

FIGURE 12. Sketch of the evolution of a bore, as modelled by the present theory. At early non-dimensional times ($t < t_2$) no shock has formed and all characteristics flow toward the right. The dotted trajectory is the position of the nose. At slightly before t_s, a shock forms at the nose if the solution is that of the limiting bore. However, for the 'bore' class of solutions, information from the shock does not flow to the left, so trajectories of characteristics to the left of the bore are unaltered.

6. Critical remarks and conclusions

A dynamically consistent model of the evolution of a coastal intrusion has been developed, starting from an initial configuration in which the distance of the front from the vertical wall varies slowly in the downstream direction. The uniqueness of (L, c) depends on an assumption, the physical significance of which may be argued in a slightly different way from that used in the text.

Suppose that at some initial time we have a front that varies slowly in $\hat{x}$ from $\hat{x} = -\infty$ to the nose point $\hat{x}_n$. We seek self-similar solutions $(\hat{u}(\hat{x}, \hat{L}(\hat{x}, \hat{t}), \hat{t}) = \hat{U}(\hat{L}))$ of the long-wave equations, subject to certain side conditions, whch will evolve into the limiting observable state. The local propagation velocities are required to decrease towards the nose, for otherwise the initial state will develop into a thinning wedge and the solution will be greatly modified by friction. The proper solution must therefore tend to develop a shock, which, according to the long-wave theory, forms first at some point (t_s, x_s) in the phase plane (figure 12). The 'early-stage' (long-wave) equations obviously cease to be uniformly valid at this point, and the more exact equations (4.1) and (4.2) must be used to continue the solution into the intermediate stage. The next stipulation for our particular solution is that there be no 'upstream influence', in the following sense. Let $x_n(t)$ be that straight line which extrapolates the nose position as computed from the early-stage equations. We then require that the solution at all (x, t)-points to the left $(x - x_n(t) < 0)$ of this line remain at the values given by the early-stage equation. Implicit here is the (theoretically) testable assumption that the early and intermediate stage can be joined in the vicinity of the line $x_n(t)$, such that the shock forms first at the nose. Otherwise, the early-stage solution will *not* be uniformly valid for all $x < x_n(t)$, and such an 'interior' shock $(x_s(t_s) < x_n(t_s))$ will not evolve as simply as the solution being proposed. As mentioned following (4.28), a shock at the nose implies that dU/dL must be finite at $L = 0$, and this boundary condition closes the early-stage problem. Although the corresponding nose speed is zero, this will be greatly modified by the later stage. The upstream width L, on the other hand, will not be altered, and we have shown how the later-stage nose velocity can be computed by an adaptation of Benjamin's theory. The mathematical existence of such a simple solution has, of course, not been proven.

The question of whether this 'limiting bore' can be realized does not depend critically upon geometrical similitude between the *initial* state of the experiment and the theory. The initial-value problem posed by the experimental set-up is theoretically intractable (in our opinion), and only the later stages of the evolution requires rationalization. We have shown that the width L of the bore that finally emerges in the dam-break experiment ($0{\cdot}42 \pm 0{\cdot}06$) is in acceptable agreement with the theoretical model. The same is true for the nose speed (5.1), and the detrainment coefficient (5.2) is also accounted for qualitatively. (The numbers are insensitive to the potential vorticity, and rather insensitive to a second layer of finite depth (see appendix C).) We therefore conclude that the limiting bore is approximately realized in the complex adjustment process that occurs at the coastal stagnation point after the dam is broken, and when a constant-velocity boundary current is found. We have no explanation as to why this should occur.

Other types of coastal intrusions (i.e. solutions) can perhaps be realized by different experimental set-ups. Experiments in basins larger than ours would be desirable to test the Reynolds-number dependence suggested by figure 8. Such experiments may show that the downstream distance $\hat{x}$ is an important dimension, as is the case in the downstream spread of a *non*-rotating turbulent jet. A statistically steady source–sink experiment in a rotating frame would be desirable to resolve the 'large' scale eddies that we see, and the averaged profiles should eliminate the subjective element that enters into our determination of the width of the boundary current.

The general aspects of density currents discussed herein may be oceanically relevant, even though coasts are not vertical (the topographical effects must be taken into account (Stern 1980, p. 701)). We have in mind the formation of surface bores during spring runoff, and the formation of abyssal bores during the intermittent flow over the sills (e.g. Denmark Straits, Anagada–Jungfern Passage, Gibraltar Straits) that separate basins with different water masses. It would be unnecessarily restrictive to regard the bore as merely a starting (transient) phenomenon. It may occur at any boundary where there are strong longshore density gradients, even when these are intermittent features of a stationary process. The longshore fronts may form and dissipate (rather quickly), with the whole process being an important part of the mean boundary current. Such is the impression we get from the experiments, wherein the fluid detrained at the nose as well as the frontal instabilities give rise to a larger-scale mean baroclinic boundary current.

A substantial portion of the work was completed while the authors were in attendance at the Summer Study Program in Geophysical Fluid Dynamics at the Woods Hole Oceanographic Institution. The program is supported by the Office of Naval Research under contract N00014-79-C0671. Some of the latest experiments were conducted with support of the Office of Naval Research contract N0001481-C-0010. The authors are grateful for the skilled laboratory assistance of Robert Frazel and want to thank Nathan Paldor for his analysis of the data. This paper is Woods Hole Oceanographic Institution Contribution no. 4824.

Appendix A. A general constraint on the width

Following the remark made at the end of §3, we now examine the consequences of assuming invariance of $\frac{1}{2}\hat{V}_c^2+f\hat{c}\hat{y}+g\hat{z}$ (3.2) on the free-surface dividing streamline. At one end $\hat{x}=-\infty$, we have $\hat{V}_c^2=(\hat{u}_\mathrm{d}-\hat{c})^2$ where $\hat{u}_\mathrm{d}$ is the f-frame velocity on the dividing streamline far upstream from the nose, and $\hat{z}_\mathrm{d}$ is the corresponding free-surface height. The datum surface for measuring the latter quantity is the parabolic level surface that passes through the undisturbed free surface at $\hat{x}=+\infty$. The dividing streamline under consideration must also pass through the nose stagnation point at which $\hat{V}_c=0$, $\hat{y}=0$, and the height is $\hat{z}=\hat{z}_\mathrm{s}$. By equating the Bernoulli functions at the two ends of the dividing streamline we get

$$\tfrac{1}{2}(\hat{u}_\mathrm{d}-\hat{c})^2+g\hat{z}_\mathrm{d}+f\hat{c}\hat{y}_\mathrm{d}=g\hat{z}_\mathrm{s}.$$

Using (3.3) to eliminate $\hat{z}_\mathrm{s}$ yields

$$\tfrac{1}{2}(\hat{u}_\mathrm{d}-\hat{c})^2+g\hat{z}_\mathrm{d}+f\hat{c}\hat{y}_\mathrm{d}=\tfrac{1}{2}\hat{c}^2.$$

Now $\hat{z}_\mathrm{d}$ is a positive number (proportional to $\hat{h}$ if the lower layer is relatively deep), and therefore the above equation gives the important inequality $f\hat{c}\,\hat{y}_\mathrm{d}<\frac{1}{2}\hat{c}^2$, which becomes

$$f\hat{y}_\mathrm{d}<\tfrac{1}{2}\hat{c}=\frac{1}{2}\frac{\displaystyle\int_0^{\hat{y}_\mathrm{d}}\hat{u}\hat{h}\,d\hat{y}}{\displaystyle\int_0^{\hat{y}_\mathrm{d}}\hat{h}\,d\hat{y}}$$

when (3.1) is used; it being understood that the integrals are evaluated at $\hat{x}=-\infty$.

The terms that have been consistently discarded in the formation of this inequality from the preceding equations are believed to be larger than the terms (unsteadiness and friction) neglected in the primitive equations, and therefore we have high confidence in the upper bound for $\hat{y}_\mathrm{d}$. This involves no far-reaching assumptions, such as have been made in the text to obtain an explicit equation for the width of the intrusion.

Since the right-hand side of the inequality is certainly less than half the maximum $\hat{u}(y)$, we conclude that the upstream Rossby number based on maximum $\hat{u}$ and $\hat{y}_\mathrm{d}$ must be *greater* than two, for a quasi-laminar bore to propagate along a coast. Initial distributions of density having widths larger than that permitted by the above inequality must therefore suffer a profound readjustment (such as bifurcation) before the density current can propagate.

If the lower layer is very deep, so that the corresponding current in the rotating frame is zero then $\hat{u}=-(\Delta\rho/\rho)\,(g/f)\,\partial\hat{h}/\partial\hat{y}$. Upon substituting this and noting the geometrical inequality

$$\int_0^{\hat{y}_\mathrm{d}}\hat{h}\,d\hat{y}>\int_0^{\hat{y}_\mathrm{d}}\hat{h}_0(1-\hat{y}/\hat{y}_\mathrm{d})\,d\hat{y},$$

where $\hat{h}_0$ is the upstream wall height, we get

$$\hat{y}_\mathrm{d}<\frac{(g^*\hat{h}_0)^{\frac{1}{2}}}{f\sqrt{2}},\quad g^*\equiv g\Delta\rho/\rho.$$

This states that the laminar bore width $\hat{y}_\mathrm{d}$ (which we interpret to be the $\hat{L}$ measured in our experiments) must be less than 0·717 times the Rossby radius of deformation.

Appendix B. Some additional features of the evolution of the solutions

Although this paper is primarily concerned with the leading edge of the intrusion, the nature of the waves that can propagate on the trailing front are also of interest. This subject has been studied by Stern (1980), for the case of zero potential vorticity, and the modifications required by a finite potential vorticity are given below.

The discussion is based on the properties of the similarity solutions (4.25)–(4.27), which will be summarized here. Typical solutions of the two Riemann-invariant families ($\pm$) of (4.25)–(4.27) are given in figure 10 for a non-dimensional potential vorticity $H = 2$, along with other auxiliary curves. A comparison with the zero-potential-vorticity case in figure 11 yields no qualitative differences.

A curve such as *PS* in both figures corresponds to propagating bores as defined by Stern in which the upstream velocities are larger than the nose speed and in which the energy flux converges towards the nose. The wedge solutions such as curve *SR* have the opposite behaviour, that is the thickness of the nose decreases with time.

The functional relation between $L(x, t)$, $U(x, t)$ and $h(x, o, t)$ is independent of time relative to an observer moving with the local propagation speed given by (4.24), and which for finite potential vorticity is given by

$$\frac{dx}{dt} = \frac{2H^{\frac{1}{2}}\left[\dfrac{U}{H^{\frac{1}{2}}}\cosh\dfrac{L}{H^{\frac{1}{2}}} - \sinh\dfrac{L}{H^{\frac{1}{2}}}\right]}{c \pm d^{\frac{1}{2}}}, \tag{B 1a}$$

$$c = 1 + \cosh\frac{L}{H^{\frac{1}{2}}},$$

$$d = \frac{2\sinh\dfrac{L}{H^{\frac{1}{2}}}\left[\left(\sinh^3\dfrac{L}{2H^{\frac{1}{2}}}\right)\dfrac{U}{H^{\frac{1}{2}}} - \cosh^3\dfrac{L}{2H^{\frac{1}{2}}} + 2\cosh\dfrac{L}{2H^{\frac{1}{2}}}\right]}{\dfrac{U}{H^{\frac{1}{2}}}\cosh\dfrac{L}{2H^{\frac{1}{2}}} - \sinh\dfrac{L}{2H^{\frac{1}{2}}}}.$$

For $H \rightarrow \infty$, one regains the zero-potential-vorticity case

$$\frac{dx}{dt} = \frac{U-L}{1 \pm (L/2U-L)^{\frac{1}{2}}}. \tag{B 1b}$$

Other curves in figures 10 and 11 that limit the regions of physical meaning are also drawn in the phase space (U, L) and are listed below.

The possible values of the upstream state of the current are given by the curve *PQR*, which is obtained by setting $h(-\infty, o, t) = 1$ in (4.11), and thus we have

$$U = \frac{1 + H\left(\cosh\dfrac{L}{H^{\frac{1}{2}}} - 1\right)}{H^{\frac{1}{2}}\sinh\dfrac{L}{H^{\frac{1}{2}}}}, \tag{B 2}$$

when $H \rightarrow \infty$ this reduces to Stern's results

$$U = \frac{1}{L} + \tfrac{1}{2}L.$$

Solutions of physical meaning must lie above the curve *OB*, which corresponds to the sections of the boundary current where the depth at the wall goes to zero, and which is obtained by setting $h(x, o, t) = 0$ in (4.11):

$$U = H^{\frac{1}{2}}\left(\tanh\frac{L}{2H^{\frac{1}{2}}}\right). \tag{B 3}$$

The limit for zero potential vorticity yields

$$U = \tfrac{1}{2}L.$$

Curve OR is the locus of sections where the flow at the wall reverses, and is found by setting $u(x, o, t) = 0$ in (4.12):

$$U = H^{\frac{1}{2}}\left(\tanh\frac{L}{H^{\frac{1}{2}}}\right). \tag{B 4}$$

The limit for $H \rightarrow \infty$ yields $U = L$.

Many of the conclusions for the zero potential vorticity are not changed for non-zero constant potential vorticity, as the illustration below for the quasi-geostrophic wave shows.

Let us consider a boundary geostrophic current with a front that lies parallel to the coast in the interval $-\infty < x < +\infty$. If the current is unidirectional, then the largest possible width will correspond to the point R in figure 10, i.e. to the value

$$L_R = H^{\frac{1}{2}} \arg\cosh\frac{H}{H-1}, \tag{B 5}$$

which is found by intersecting the upstream-state curve (B 2) with the locus of sections where the flow reverses at the wall (B 4). If this basic state is perturbed by a wavelike motion corresponding to a similarity solution such as the (+) Riemann invariant passing through R, then the local propagation speed (B 1*a*) will have opposite signs for sections of the boundary current lying on each side of curve OR, i.e. for a width $L >$ or $< L_R$. If $L > L_R$, then the local propagation speed (B 1*a*) will be negative since $U_{(+)}$ (L) lies below the curve OR and will increase in magnitude as $L - L_R$ increases. Therefore, the front will steepen on the upstream side of the wave and the amplitude dispersion depending on the boundary-current width will lead to a backwards-breaking wave. Moreover, one can verify from the expression of the transverse velocity dL/dt along the streamline,

$$v = \frac{\partial L}{\partial t} + U\frac{\partial L}{\partial x} = \frac{U}{1-U'}\frac{\partial L}{\partial x},$$

and by evaluating $\partial h/\partial x$ from (4.11),

$$\frac{\partial h}{\partial x} = \left[-H^{\frac{1}{2}}\sinh\frac{L-y}{H^{\frac{1}{2}}} + U\cosh\frac{L-y}{H^{\frac{1}{2}}}\right]\frac{\partial L}{\partial x},$$

that $v \simeq [\partial h/\partial x]_{y=L}$ at point R (since $U' \simeq 0$) and the wavelike motion is quasi-geostrophic for both longitudinal and transverse velocities. Thus the discussion above is independent of the finite value of constant potential vorticity, and the generalization of 'the other waves and blocking waves' as discussed by Stern (1980) is also straightforward.

Appendix C. The effect of the finite bottom-layer depth

Although the thickness of the heavy fluid in our experiments was an order of magnitude larger than the thickness of the intrusion, there will be some vertical compression of the heavy fluid columns as the bore passes over them, and it is of interest to investigate the feedback. For this purpose the rigid bottom of the tank is assumed to be a level surface so that the fluid in advance of the nose has uniform thickness and a uniform potential vorticity. The non-dimensional value of the latter is denoted by $1/H_2$, whereas $1/H_1$ now denotes the potential vorticity of the upper layer; both of these being based on h_0 as the unit of height. If $P_1(x, y, t)$ denotes the pressure on the upper $z = 0$ surface, and $P_2(x, y, t)$ the pressure on the bottom surface, then the generalization of (4.7) and (4.8) to the two-layer case is

$$\left.\begin{aligned} u_{1t}-(1-u_{1y})\,v_1 &= -(p_1+\tfrac{1}{2}u_1^2)_x, \\ u_{2t}-(1-u_{2y})\,v_2 &= -(p_2+\tfrac{1}{2}u_2^2)_y, \end{aligned}\right\} \tag{C 1}$$

$$u_1 = -(p_1)_y, \quad u_2 = -(p_2)_y. \tag{C 2}$$

The hydrostatic relation connects the upper-layer thickness h with the pressure gradients:

$$\nabla p_1 - \nabla p_2 = \nabla h, \tag{C 3}$$

and thus the elimination of p_1 and p_2 in (C 1) and (C 2) gives

$$(u_1-u_2)_t-[(1-u_{1y})\,v_1-(1-u_{2y})\,v_2] = -(h+\tfrac{1}{2}u_1^2-\tfrac{1}{2}u_2^2)_x, \tag{C 4}$$

$$(u_1-u_2) = -h_y. \tag{C 5}$$

The continuity relations for the two layers are

$$h_t+(hu_1)_x+(hv_1)_y = 0, \tag{C 6}$$

$$-h_t+[(H_2-h)u_2]_x+[(H_2-h)v_2]_y = 0, \tag{C 7}$$

and the potential-vorticity equations are

$$\frac{1-u_{1y}}{h} = \frac{1}{H_1}, \tag{C 8}$$

$$\frac{1-u_{2y}}{H_2-h} = \frac{1}{H_2}. \tag{C 9}$$

The top layer extends from $y = 0$ to $y = L(x, t)$, where $h = 0$, whereas the bottom layer extends from $y = 0$ to $y = \infty$ with a non-analytic behaviour at $y = L(x, t)$. The circulation theorem precludes a vortex sheet in the heavy fluid, and thus u_2 must be continuous on either side of the front. Moreover (C 9) implies $u_{2_y} = 0$ for all $y \geqslant L$, and therefore

$$\frac{\partial u_2}{\partial y} = 0 = u_2 \quad \text{at} \quad y = L(x, t), \tag{C 10}$$

for otherwise u_2 would be infinite at $y = \infty$.

The solutions of (C 5), (C 8) and (C 9) that satisfy the $y = L$ boundary conditions (C 10) are

$$h(x,y,t) = H\left(1-\cosh\frac{L-y}{H^{\frac{1}{2}}}\right)+H^{\frac{1}{2}}U\sinh\frac{L-y}{H^{\frac{1}{2}}}, \tag{C 11}$$

$$u_1(x,y,t) = \frac{H}{H_2}(y-L+U)+\frac{H}{H_1}\left(-H^{\frac{1}{2}}\sinh\frac{L-y}{H^{\frac{1}{2}}}+U\cosh\frac{L-y}{H^{\frac{1}{2}}}\right), \qquad \text{(C 12)}$$

$$u_2(x,y,t) = \frac{H}{H_2}(y-L+U)-\frac{H}{H_2}\left(-H^{\frac{1}{2}}\sinh\frac{L-y}{H^{\frac{1}{2}}}+U\cosh\frac{L-y}{H^{\frac{1}{2}}}\right), \qquad \text{(C 13)}$$

where

$$H \equiv \frac{H_1 H_2}{H_1+H_2}$$

now denotes an 'equivalent depth', and $U = u_1(x, L, t)$ as previously.

To obtain the long-wave equations for (U, L) we will evaluate (C 4) on $y = L$ where $\partial u_1/\partial y = 1$, $\partial u_2/\partial y = u_2 = 0$, and therefore

$$[(u_1-u_2)_t]_{y=L}+[(h+\tfrac{1}{2}u_1^2)_x]_{y=L}+[v_2]_{y=L} = 0. \qquad \text{(C 14)}$$

We will also use the integrated version of (C 6) and (C 7), or

$$\left.\begin{aligned} \int_0^{L(x,t)} h_t\,dy+\int_0^{L(x,t)}(hu_1)_x\,dy &= 0,\\ -\int_0^{L(x,t)} h_t\,dy+\int_0^{L(x,t)}((H_2-h)u_2)_x\,dy+[H_2v_2]_{y=L} &= 0. \end{aligned}\right\} \qquad \text{(C 15)}$$

Eliminating between (C 14) and (C 15) gives the following system:

$$\begin{aligned} [(u_1-u_2)_t]_{y=L}+[(h+\tfrac{1}{2}u_1^2)_x]_{y=L}+\frac{1}{H_2}\int_0^{L(x,t)} h_t\,dy&\\ -\int_0^{L(x,t)} u_{2x}\,dy+\frac{1}{H_2}\int_0^{L(x,t)}(hu_2)_x\,dy &= 0, \end{aligned} \qquad \text{(C 16)}$$

$$\frac{\partial}{\partial t}\int_0^{L(x,t)} h\,dy+\frac{\partial}{\partial x}\int_0^{L(x,t)} hu_1\,dy = 0. \qquad \text{(C 17)}$$

When the profiles of $u_1(x, y, t)$, $h(x, y, t)$ and $u_2(x, y, t)$ given by (C 11)–(C 13) are used to evaluate the above terms, and when the result is simplified, we get

$$\begin{aligned} &\left(\frac{U}{H}\sinh\frac{L}{H^{\frac{1}{2}}}\right)\frac{\partial L}{\partial t}\\ &+\left\{\left(\cosh\frac{L}{H^{\frac{1}{2}}}-1\right)\left(\frac{U}{H^{\frac{1}{2}}}\cosh\frac{L}{H^{\frac{1}{2}}}-\sinh\frac{L}{H^{\frac{1}{2}}}\right)\left[1+\frac{H}{H_2}\left(\cosh\frac{L}{H^{\frac{1}{2}}}-1\right)\right]\right\}\frac{\partial U}{\partial x}\\ &+\left\{\left(\frac{U}{H^{\frac{1}{2}}}\sinh\frac{L}{H^{\frac{1}{2}}}-\cosh\frac{L}{H^{\frac{1}{2}}}+1\right)\left(\frac{U}{H^{\frac{1}{2}}}\cosh\frac{L}{H^{\frac{1}{2}}}-\sinh\frac{L}{H^{\frac{1}{2}}}\right)\left(1+\frac{H}{H_2}\left(\cosh\frac{L}{H^{\frac{1}{2}}}-1\right)\right)\right.\\ &\left.+\frac{H}{H_2}\frac{U}{H^{\frac{1}{2}}}\sinh\frac{L}{H^{\frac{1}{2}}}\left(\frac{U}{H^{\frac{1}{2}}}-\frac{L}{H^{\frac{1}{2}}}-\left(\frac{U}{H^{\frac{1}{2}}}\cosh\frac{L}{H^{\frac{1}{2}}}-\sinh\frac{L}{H^{\frac{1}{2}}}\right)\right)\right\}\frac{\partial L}{\partial x} = 0, \end{aligned} \qquad \text{(C 18)}$$

$$\begin{aligned} &\frac{\partial U}{\partial t}-\frac{\partial L}{\partial t}+\frac{\partial U}{\partial x}\left\{U-\frac{H}{H_2}H^{\frac{1}{2}}\left[\frac{L}{H^{\frac{1}{2}}}+\sinh\frac{L}{H^{\frac{1}{2}}}\left(\frac{U}{H^{\frac{1}{2}}}\sinh\frac{L}{H^{\frac{1}{2}}}-\cosh\frac{L}{H^{\frac{1}{2}}}\right)\right]\right\}\\ &+\frac{\partial L}{\partial x}\frac{H}{H_2}H^{\frac{1}{2}}\left[\frac{L}{H^{\frac{1}{2}}}-\tfrac{1}{2}\sinh\frac{2L}{H^{\frac{1}{2}}}-\frac{U}{H^{\frac{1}{2}}}\sinh\frac{L}{H^{\frac{1}{2}}}\left(\frac{U}{H^{\frac{1}{2}}}\cosh\frac{L}{H^{\frac{1}{2}}}-2\sinh\frac{L}{H^{\frac{1}{2}}}\right)\right] = 0. \end{aligned} \qquad \text{(C 19)}$$

One can verify that for $H/H_2 \rightarrow 0$, i.e. in the case of a boundary current overlying an infinitely deep second layer, (C 18) and (C 19) are identical with the system found in §4, (4.15) and (4.13) respectively. Terms multiplying H/H_2, i.e. due to the coupling of the bore with a second layer of *finite depth*, give an extra contribution of order L^2/H_2 for small $L/H^{\frac{1}{2}}$.

The similarity solutions satisfying the functional relation (4.20) obey the ordinary differential equation

$$\frac{dU}{dL} = 1 - \frac{2\dfrac{U}{H^{\frac{1}{2}}}\cosh\dfrac{L}{2H^{\frac{1}{2}}}\left[1 - \dfrac{H}{H_2}\sinh\dfrac{L}{H^{\frac{1}{2}}}\left(\dfrac{U}{H^{\frac{1}{2}}}\cosh\dfrac{L}{H^{\frac{1}{2}}} - \sinh\dfrac{L}{H^{\frac{1}{2}}}\right)\right]}{a \pm (a^2+b)^{\frac{1}{2}}}, \qquad \text{(C 20)}$$

$$a = \sinh\frac{L}{H^{\frac{1}{2}}}\left[\cosh\frac{L}{2H^{\frac{1}{2}}} - \frac{U}{H^{\frac{1}{2}}}\sinh\frac{L}{2H^{\frac{1}{2}}} - 2\frac{H}{H_2}\sinh\frac{L}{2H^{\frac{1}{2}}}\left(\frac{U}{H^{\frac{1}{2}}}\cosh\frac{L}{H^{\frac{1}{2}}} - \sinh\frac{L}{H^{\frac{1}{2}}}\right)\right], \qquad \text{(C 21}a\text{)}$$

$$\begin{aligned} b = 2\sinh\frac{L}{H^{\frac{1}{2}}}\left(\frac{U}{H^{\frac{1}{2}}}\cosh\frac{L}{H^{\frac{1}{2}}} - \sinh\frac{L}{H^{\frac{1}{2}}}\right) & \\ \times\left\{1 + \frac{H}{H_2}\left[\cosh\frac{L}{H^{\frac{1}{2}}} - 1 + \sinh\frac{L}{H^{\frac{1}{2}}}\left(\frac{U}{H^{\frac{1}{2}}}\cosh\frac{L}{H^{\frac{1}{2}}} - \sinh\frac{L}{H^{\frac{1}{2}}}\right)\right]\right. & \\ \left. -\left(\frac{H}{H_2}\right)^2\sinh\frac{L}{H^{\frac{1}{2}}}\left(\cosh\frac{L}{H^{\frac{1}{2}}} - 1\right)\left(\frac{U}{H^{\frac{1}{2}}}\cosh\frac{L}{H^{\frac{1}{2}}} - \sinh\frac{L}{H^{\frac{1}{2}}}\right)\right\} & \qquad \text{(C 21}b\text{)} \end{aligned}$$

When putting $H/H_2 = 0$ in (C 20) and (C 21), we recover the system found for an infinitely deep second layer, (4.25) and (4.26). Again the leading terms in an expansion in $L/H^{\frac{1}{2}}$ in (C 20) near $L = 0$ are identical with those previously found for the zero-potential-vorticity case. Therefore the discussion concerning the nose boundary condition still applies, i.e. we need $U(0) = 0$.

The upstream width of this simple bore will be found by integrating (C 20) using (4.29), and by finding the intersection with the upstream-state curve

$$U = \frac{1 + H\left(\cosh\dfrac{L}{H^{\frac{1}{2}}} - 1\right)}{H^{\frac{1}{2}}\sinh\dfrac{L}{H^{\frac{1}{2}}}} \qquad \text{(C 22)}$$

obtained by setting $h(-\infty, 0, t) = 1$ in (C 11).

Table 3 gives $L(-\infty)$ as a function of the initial equivalent depth H and the ratio H/H_2. However, for a given H, not all values of H/H_2 are allowed, since $H_2 \geqslant 1$ and $H_1 \geqslant 1$. The entire range of $L(-\infty)$ in table 3 is

$$0{\cdot}418 \leqslant L(-\infty) \leqslant 0{\cdot}516, \qquad \text{(C 23)}$$

and thus the coupling with a second layer may increase the width of the boundary current up to 25 %. The largest values of $L(-\infty)$ are found for small H ($0{\cdot}5 < H < 1$), i.e. for values of both H_1 and H_2 close to 1. The maximum of $L(-\infty)$ is reached for $H = 0{\cdot}5$ ($H_1 = 1$ and $H_2 = 1$).

However, interesting values of H_1 and H_2 would be closer to 2 (remember that the upstream height has been chosen for normalizing the heights) and in this range the width of the boundary current remains within 10 % of the value found for the very simplest case of one layer with zero potential vorticity. The new profiles of current

H \ H/H_2	0·1	0·3	0·5	0·7	0·9
0·5	—	—	0·516	—	—
0·75	—	0·450	0·470	0·496	—
1	0·431	0·442	0·454	0·469	0·488
2	0·425	0·429	0·435	0·440	0·446
10	0·420	0·421	0·422	0·422	0·423

TABLE 3. Values of upstream width $L(-\infty)$ as a function of initial equivalent depth H and of ratio H/H_2

given by (C 11)–(C 13) have also been used to evaluate the nose speed c and the detrainment coefficient δ. For the upstream wall velocity we have

$$u_1 = \frac{H}{H_2}(U-L)+\frac{H}{H_1}\,\frac{(1-H)\cosh\dfrac{L}{H^{\frac{1}{2}}}+H}{H^{\frac{1}{2}}\sinh\dfrac{L}{H^{\frac{1}{2}}}} \quad \text{at} \quad x=-\infty, \quad y=0, \tag{C 24}$$

where U is defined by the upstream condition (C 22). The other quantities $\int h\,dy$ and $\int hu\,dy$ needed for (δ, c) have the same formal expression as (5.5) and (5.4) respectively, but in this case H is the initial equivalent depth. Choosing $H_1 = H_2 = 2$ and $L(-\infty) = 0{\cdot}43$ yields for c and δ

$$c = 1{\cdot}56, \tag{C 25}$$

$$\delta = 0{\cdot}34. \tag{C 26}$$

Again we conclude that the bore speed seems to be independent of the structure of the current.

REFERENCES

BRITTER, R. E. & SIMPSON, J. E. 1978 Experiments on the dynamics of a gravity current head. *J. Fluid Mech.* **88**, 223–240.

BENJAMIN, T. B. 1968 Gravity currents and related phenomena. *J. Fluid Mech.* **31**, 209–248.

GRIFFITHS, R. W. & LINDEN, P. F. 1981 The stability of vortices in a rotating, stratified fluid. *J. Fluid Mech.* **105**, 283–316.

HODGMAN, C. D. (ed.) 1961 *Handbook of Chemistry and Physics*, 43rd edn. Chemical Rubber.

KÁRMÁN, T. v. 1940 The engineer grapples with nonlinear problems. *Bull. Am. Math. Soc.* **46**, 615.

SAUNDERS, P. M. 1973 The instability of a baroclinic vortex. *J. Phys. Oceanogr.* **3**, 61–65.

SIMPSON, J. E. & BRITTER, R. E. 1979 The dynamics of the head of a gravity current advancing over a horizontal surface. *J. Fluid Mech.* **94**, 477–495.

STERN, M. E. 1975 *Ocean Circulation Physics*. Academic.

STERN, M. E. 1980 Geostrophic fronts, bores, breaking and blocking waves. *J. Fluid Mech.* **99**, 687–703.

WADHAMS, P., GILL, A. E. & LINDEN, P. F. 1979 Transects by submarine of the east Greenland polar front. *Deep-Sea Res.* **26A**, 1311–1327.